Quantum-statistical theory for laser-tuned transport and optical conductivities of dressed electrons in α−T_{3} materials

Andrii Iurov, Liubov Zhemchuzhna, Dipendra Dahal, Godfrey Gumbs, and Danhong Huang

Quantum-statistical theory for laser-tuned transport and optical conductivities of dressed electrons in $\alpha - \mathcal{T}_3$ materials

Andrii Iurov[1,2*], Liubov Zhemchuzhna[3], Dipendra Dahal[3], Godfrey Gumbs[3,4], and Danhong Huang[5,2]

[1]*Department of Physics and Computer Science, Medgar Evers*
College of City University of New York, Brooklyn, NY 11225, USA
[2]*Center for High Technology Materials, University of New Mexico,*
1313 Goddard SE, Albuquerque, New Mexico, 87106, USA
[3]*Department of Physics and Astronomy, Hunter College of the City University of New York,*
695 Park Avenue, New York, New York 10065, USA
[4]*Donostia International Physics Center (DIPC),*
P de Manuel Lardizabal, 4, 20018 San Sebastian, Basque Country, Spain
[5]*Air Force Research Laboratory, Space Vehicles Directorate,*
Kirtland Air Force Base, New Mexico 87117, USA
(Dated: December 23, 2019)

In the presence of external off-resonance and circularly-polarized irradiation, we have derived a many-body formalism and performed a detailed numerical analysis for both the conduction and optical currents in $\alpha - \mathcal{T}_3$ lattices. The calculated complex many-body dielectric function, as well as conductivities of displacement and transport currents, display strong dependence on the lattice-structure parameter α, especially approaching the graphene limit with $\alpha \to 0$. Unique features in dispersion and damping of plasmon modes are observed with different α values, which are further accompanied by a reduced transport conductivity under irradiation. The discovery in this paper can be used for designing novel multi-functional nanoelectronic and nanoplasmonic devices.

I. INTRODUCTION

So far, the $\alpha - \mathcal{T}_3$ model seems to present prospective opportunities for a new surge of noticeable progress in low-dimensional physics through novel two-dimensional (2D) materials [1]. Its atomic configuration consists of a graphene-type honeycomb lattice along with an additional site, i.e., a hub atom at the center of each hexagon.[2] An essential structure parameter $\alpha = \tan\phi$, which enters into the low-energy Dirac-Weyl pseudospin-1 Hamiltonian for $\alpha - \mathcal{T}_3$ model, is found to be the ratio between the rim-to-hub and rim-to-rim hopping coefficients. This parameter affects all fundamental electronic properties of the $\alpha - \mathcal{T}_3$ lattice through topological characteristics embedded in its pseudospin-1 wave functions. Parameter α can vary from 0 to 1, corresponding to different types of $\alpha - \mathcal{T}_3$ materials, and the control of it could lead to some important technological applications for electronic and optoelectronic devices. Here, the case with $\alpha = 0$ relates to graphene with a completely separated flat band, whereas $\alpha = 1$ results in a pseudospin-1 dice lattice which has been fabricated and studied considerably. [3, 4] Consequently, the $\alpha - \mathcal{T}_3$ model may be viewed as an interpolation between graphene and the dice lattice (or pseudospin-1 $\mathcal{T}_3$ model). Its low-energy dispersion consists of a Dirac cone, similar to that for graphene, [5] as well as a flat band with zero-energy separating the valence from the conduction band for these pseudospin-1 materials. [6, 7]

In recent years, there have been numerous attempts for experimental realization of the $\alpha - \mathcal{T}_3$ model. Its topological characteristics, i.e., a Dirac cone with three bands touching at a single point, was observed in the triplon band structure of $SrCu_2(BO_3)_2$, as an example of general Mott-Hubbard insulators [8]. One of the first artificial nanoscale lattices was engineered using atomic manipulation and lithographic techniques, as described in Ref. [9]. Another example of dice lattice is a naturally built trilayer heterostructure based on transition-metal oxides such as $SrTiO_3$ [4]. The Kagome lattice in which additional atoms are located in the middle of each side of a hexagon [10, 11] was realized experimentally in 2012 as presented in Ref. [12] by achieving interference between two triangular lattices. We note that flat bands have also been presented in photonics by using slow light [13] with a reduced group velocity of light, leading to stronger nonlinear optical effects. Moreover, dielectric photonic crystals with zero refractive index also display Dirac cone dispersion at the center of the Brillouin zone under an accidental degeneracy. [14, 15] Most importantly, there exist various types of photonic Lieb lattices, [16, 17] consisting of a 2D array of optical waveguides. Such waveguide-lattice structure is shown to have a three-band structure, including a perfectly flat middle band. A particularly explicit review and summary of all known existing lattices with a flat energy band can be found in Ref. [18].

---

* E-mail contact: aiurov@mec.cuny.edu, theorist.physics@gmail.com

Further to a relatively recent proposal on $\alpha - \mathcal{T}_3$ model, there have been a lot of crucial publications devoted to investigating their magnetic, [1, 19–21] optical, [22] many-body [7] and electron transport properties, [23–26], as well as to generalized versions of this model [27]. The $\alpha - \mathcal{T}_3$ model displays unique and remarkable topological properties and breaks down some symmetries which were not found in previously discovered Dirac materials. In the current case, circularly polarized light can lift the degeneracy at the Dirac point and the irradiated lattice changes from a semimetal to a Haldane-like Chern insulator [28]. A number of compelling properties of graphene and other low-dimensional materials [29] have been realized in $\alpha - \mathcal{T}_3$ materials, including Klein tunneling [30, 31] and Hofstadter butterfly [31] in comparison to that in graphene [32]. Meanwhile, all pseudospin-1 structures also display some previously unknown phenomena resulting from the existence of a flat band in their energy dispersions [33], e.g., distinctive plasmon modes with a branch "*pinching*" feature at the Fermi level. [7]

It was shown that in black phosphorous with highly anisotropic energy subbands the plasmon dispersions are also anisotropic and scale with the doping density (n) as n^β with $\beta < 1/2$ [34]. These results are particularly relevant to an investigation of plasmons in the dressed states since the anisotropy in $\alpha - \mathcal{T}_3$ could be induce by applying elliptically-polarized light which is the most general case for the polarization of an optical dressing field. An investigation of how a vertical electric field affects the electronic band structure and transport properties of multilayer phosphorene and corresponding nanoscale ribbons was performed in Ref. [35] It was shown [36] that distinct valley populations in transition metal dichalcogenidessuch as WSe_2, could be optically induced under a very weak magnetic field. It was also demonstrated that the already inefficient relaxation of the exciton pseudospin is further weakened by this magnetic field so that pseudospin dynamics displays a two-step relaxation process. At a specific electric field, the bandgap becomes closed, which appears as an opposite effect in comparison with opening a band gap in $\alpha - \mathcal{T}_3$ materials by circularly-polarized irradiation. Ref. [37] describes two-dimensional optics as a new and important part of modern optical science. By squeezing light into an atomic scale, two-dimensional optics could be realized in graphene through plasmons. This technique could also apply to pseudospin-1 $\alpha - \mathcal{T}_3$ materials. By using Floquet theory, electronic and transport properties of a semi-Dirac material with different hopping parameters in a hexagonal lattice were studied under a temporally-periodic driving field. The light-induced bandgap depends on propagation direction of light with respect to a surface normal for a momentum transfer and reveals some unusual features in the high-frequency limit.

We note that an exciting emergent technical application for condensed-matter quantum optics is *Floquet engineering*. This subject leads to a wide-range optical-tuning capability and control of electron optical and transport currents in 2D materials by introducing an off-resonant periodic dressing field in either terahertz or microwave frequency. [38–44] Such external irradiation imposed on a 2D material produces a dramatic change in most of its electronic properties due to creating so-called *dressed states*. Thisgives rise to a single quantum entity, consisting of an electron interacting with a photon. It is described by unique energy-dispersion relations, depending on the intensity and polarization of incoming radiation.

Our investigation of such electron dressed states is based on Floquet theory for quantum systems, driven by external periodic potentials. This results in a $\backsim 1/(\hbar\omega)$ series expansion, as employed by Floquet-Magnus, Brillouin-Wigner and others, [45] and provides an effective analytical tool for investigating light-electron interaction in a variety of novel 2D materials [46–49] and optically-induced topological surface states [50] as well.

The modifications of single-particle band structure and wave function greatly affect the many-body dielectric function [29, 51, 52] in addition to electron conduction current [53, 54] and conductivity [55]. These changes mainly come from opening an energy gap [46] between the valence and conduction bands, as well as from topologically-modified wave functions. [56] For a linearly-polarized optical dressing field, we find strong in-plane anisotropy, and even the anisotropic dispersion of phosphorene still experiences a lot of changes under this dressing field. [57]

Once Floquet engineering has been applied to $\alpha - \mathcal{T}_3$ materials, we expect some fundamental changes will occur, such as, band-dispersion anisotropy, opening inequivalent energy gaps within each band, breaking down the electron-hole symmetry and valley degeneracy, [22] and topological variation of electron wave functions including their symmetries and the Berry phases. [58] Interestingly, circularly-polarized radiation can induce a topological phase transition from a gapless semimetal to a topological insulator with a nonzero Chern number. [28] This result acquires a resemblance to a topological insulator, obtained from a periodic array of quantum rings under a circularly-polarized optical field. [59]

The rest of this paper is organized as follows. In Sec. II, electron dressed states by an strong laser field in $\alpha - \mathcal{T}_3$ materials are derived. In Sec. III, the effects of optically-dressed states on many-body dielectric function, plasmon mode and electron optical current are presented. The dressed-state effects on rate for elastic impurity scattering and conduction current are displayed in Sec. IV. Finally, a summary and some remarks are given in Sec. V.
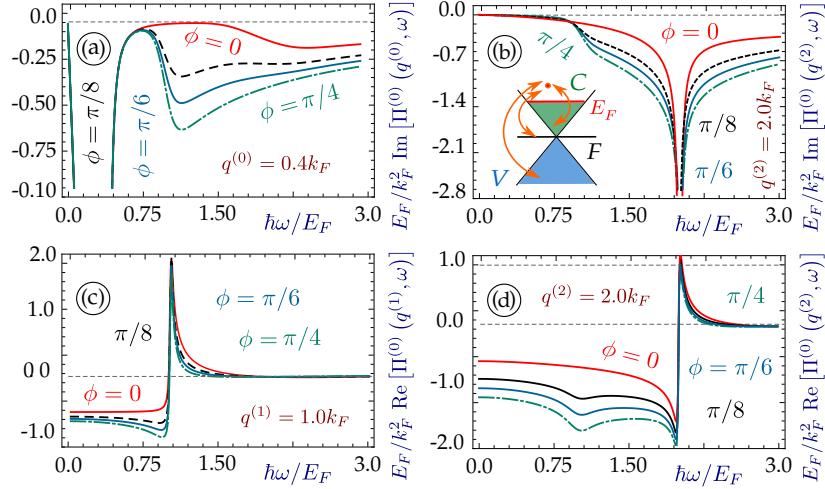
FIG. 1: (Color online) Frequency (ω) and wavevector (q) dependent polarization function $\Pi_0(q, \omega \,|\, \phi)$ (in units of k_F^2/E_F) for non-irradiated $\alpha - \mathcal{T}_3$ model ($\lambda_0 = 0$) as a function of $\hbar\omega$ with various phase values ϕ. Here, each panel corresponds to a chosen wavevector $q = q_i$ and each curve is for a specific phase ϕ, as labeled. Two upper panels [(a), (b)] present the imaginary part of $\Pi_0(q, \omega \,|\, \phi)$, whereas the two lower ones [(c), (d)] are its real part. The inset in plot (b) illustrates all possible single-particle transitions (red double-arrow curves) contributing to $\Pi_0(q, \omega \,|\, \phi)$ at $T = 0\,\mathrm{K}$ with a horizontal red line for the Fermi energy E_F.

II.   VALLEY-SPIN DEPENDENT DRESSED STATES

The optical current of electrons in $\alpha - \mathcal{T}_3$ materials should be driven by a laser field. In the presence of the laser field, bare electron states are obtained by substituting the electron wavevector $\boldsymbol{k} = \{k_x, k_y\}$ in the Hamiltonian of considered materials with $\boldsymbol{k} - (e/\hbar)\,\boldsymbol{A}(t)$. Here, $\boldsymbol{A}(t) = (\mathcal{E}_0/\omega)\,\{\cos(\omega t), \sin(\omega t)\}$ is a spatially-uniform vector potential associated with the applied circularly-polarized light, where $\mathcal{E}_0$ is the amplitude of the electric-field component of imposed radiation and ω is its angular frequency in the off-resonance regime. As a result, the Hamiltonian will acquire an additional time-dependent term due to light-electron interaction.

In this paper, we employ the Floquet-Magnus perturbation-expansion theory for our calculations. This procedure is applicable to any periodically-driven quantum structure [45] so as to obtain valley-degenerate, isotropic and symmetric energy bands near the flat band,[58] yielding $\varepsilon_0(k, \lambda_0) = 0$ and

$$\varepsilon_\gamma(k, \lambda_0) = \gamma\sqrt{\left(\lambda_0 c_0/2\right)^2 + \left[\hbar v_F k \left(1 - \lambda_0^2/4\right)\right]^2} \;, \tag{1}$$

where $\gamma = \pm$ for electrons ($+$) and holes ($-$), $c_0 = e\mathcal{E}_0 v_F/\omega$ represents the interaction coefficient (energy), v_F is the Fermi velocity, and $\lambda_0 = c_0/(\hbar\omega) = e\mathcal{E}_0 v_F/(\hbar\omega^2)$ is a dimensionless light-electron coupling parameter. We limit our consideration to off-resonance frequencies of the laser field, where the photon energy $\hbar\omega$ greatly exceeds any electron energies, e.g., Fermi energy $E_F = \hbar v_F k_F$ with the Fermi wavenumber $k_F = \sqrt{\pi\rho_0}$ and areal doping density ρ_0. Consequently, we have $\lambda_0 \ll 1$ in spite of the light intensity $\mathbb{I}_0 = \epsilon_0 c\mathcal{E}_0^2/2 \backsim 10\,W/cm^2$.

The obtained dispersions in Eq. (1) reveal an energy bandgap $E_G = \lambda_0 c_0 \equiv 2\Delta_0$ which is only half of the graphene gap energy with the same interaction coefficient c_0. [46] The electronic states for an irradiated dice lattice, pertaining to the valence and conduction bands, are given by

$$\Psi_\gamma^\tau(\boldsymbol{k}, \lambda_0) = \frac{1}{\sqrt{\mathcal{N}_\gamma^\tau}} \begin{bmatrix} \tau\,\mathcal{C}_{1,\gamma}^\tau\,\mathrm{e}^{-i\tau\theta_{\mathbf{k}}} \\ \mathcal{C}_{2,\gamma}^\tau \\ \tau\left(\hbar v_F k\right)^2 \mathrm{e}^{+i\tau\theta_{\mathbf{k}}} \end{bmatrix} , \tag{2}$$

where

$$\mathcal{C}_{1,\gamma}^\tau(k,\lambda_0) = (\hbar v_F k)^2 + 2\left(\delta_\lambda^2 - \gamma\,\tau\delta_\lambda\sqrt{(\hbar v_F k)^2 + \delta_\lambda^2}\right)\;, \tag{3}$$

$$\mathcal{C}_{2,\gamma}^\tau(k,\lambda_0) = \sqrt{2}\,\gamma\,(\hbar v_F k)\left(\sqrt{(\hbar v_F k)^2 + \delta_\lambda^2} - \gamma\,\tau\delta_\lambda\right)\;,$$

$$\mathcal{N}_\gamma^\tau(k,\lambda_0 \ll 1) \simeq 4\,(\hbar v_F k)^4 - 4\gamma\,\tau\,c_0\lambda_0\,(\hbar v_F k)^3 + 3\left[c_0\lambda_0\,(\hbar v_F k)\right]^2 + \cdots\;.$$

Here, the parameter $\delta_\lambda = 2\lambda_0 c_0/(4-\lambda_0^2)$ is different from the actual energy gap $E_G = \lambda_0 c_0 = 2\Delta_0$. For the flat band with $\gamma = 0$, on the other hand, three components of its wave function are not the same and the middle one is nonzero, as expected for a finite energy gap (see Appendix A).

Actually, irradiated dice lattice, or an arbitrary $\alpha - \mathcal{T}_3$ material, is a typical example of a *valley filter*. The laser-renormalized eigenstates and their overlaps depend on valley index in a non-trivial way with a non-cancellable contribution. Consequently, a valley averaging must be performed to take into account this difference when calculating polarization function, plasmon energies and conductivities. The electronic states, corresponding to K and K' valleys, are modified quite differently by circularly-polarized irradiation due to symmetry breaking.

The above electron dressed states share a similarity with an irradiated dice material but are not equivalent to those from a gapped Hamiltonian with an added $\Delta_0\hat{\Sigma}_z^{(3)}$ term, where $\hat{\Sigma}_z^{(3)}$ represents a (3×3) z-Pauli matrix with the main diagonal $\{1,0,-1\}$ and isused to describe the effect of a point defect. [33]

III. PLASMON MODE AND OPTICAL CURRENT

The self-sustaining charge-density longitudinal oscillations, i.e., plasmons, play an important role in determining the optical-current properties of low-dimensional structures. [29, 56, 60–62] These include exotic fullerenes and spherical graphitic particles. [63–65]

The dispersion relation of plasmon modes in the wavevector-frequency (q,ω)-plane is generally determined from the zero of a dielectric function $\epsilon(q,\omega\,|\,\phi,\lambda_0)$. In terms of the dynamical polarization function $\Pi_0(q,\omega\,|\,\phi,\lambda_0)$, we can write $\epsilon(q,\omega\,|\,\phi,\lambda_0) = 1 - (2\pi\alpha_0/q)\,\Pi_0(q,\omega\,|\,\phi,\lambda_0)$, where $\alpha_0 = e^2/(4\pi\epsilon_0\epsilon_r)$, ϵ_r is the host-material dielectric constant, and the summation over the valley index τ is performed.

The dynamical polarization function $\Pi_0(q,\omega\,|\,E_F)$ for pseudospin-1 $\alpha-\mathcal{T}_3$ at zero temperature could be determined in the one-loop approximation, yielding [7]

$$\Pi_0(q,\omega\,|\,E_F) = \frac{1}{\pi^2}\int d^2\boldsymbol{k}\sum_{\gamma,\gamma'=0,\pm1}\mathbb{O}_{\gamma,\gamma'}(\boldsymbol{k},\boldsymbol{k}+\boldsymbol{q}\,|\,\phi)\,\frac{\Theta[E_F-\varepsilon_\gamma(k)]-\Theta[E_F-\varepsilon_{\gamma'}(|\boldsymbol{k}+\boldsymbol{q}|)]}{\hbar(\omega+i0^+)+\varepsilon_\gamma(k)-\varepsilon_{\gamma'}(|\boldsymbol{k}+\boldsymbol{q}|)}\;, \tag{4}$$

where the Heaviside unit step function $\Theta(x)$ comes from the thermal-equilibrium distribution function at $T=0$ and $\varepsilon_\gamma(k)$ represents the energy dispersions of the irradiated dressed states given in Eq. (1), and $\mathbb{O}_{\gamma,\gamma'}(\boldsymbol{k},\boldsymbol{k}+\boldsymbol{q}\,|\,\phi)$ is the wave-function overlap (B1) presented in Appendix B. The wave-function overlap depends explicitly on the valley index τ. The energy dispersions for a dice lattice ($\alpha=1$) do not depend on τ, however, this is not the case for general $\alpha-\mathcal{T}_3$ materials.

The most different aspect between Eq. (4) and the case for graphene is the inclusion of the flat band in the summation over band index $\gamma,\gamma' = \{-1,0,1\}$, as schematically demonstrated in Fig.1 (b). This reveals a substantial difference between the plasmons in a dice lattice and in graphene, and such a difference is further modified by an applied dressing field. We consider electron doping with the Fermi energy $E_F > 0$ above the Dirac point. Our approach presented in Eq. (4) becomes valid only if E_F is separated from the flat band or $E_F \neq 0$. Due to the fact that both the valence and flat band are completely filled, from Eq. (4) we can exclude transitions $-1 \leftrightarrow -1$ and $0 \leftrightarrow -1$. As a result, the γ and γ' double summations *reduce to six nonzero terms* in comparison with four nonzero terms for graphene. As $\alpha \to 0$, all the wave-function overlap terms approach zero regardless of the presence or absence of irradiation.

In addition, we also require $\Pi_0(q,\omega\,|\,\phi,\lambda_0)$ in calculating screening to impurity scattering for electron conduction current. The screened potential for a dilute distribution of impurities embedded in a dice lattice has been discussed [7] as well as for general $\alpha-\mathcal{T}_3$ materials. [66] Furthermore, we notice $\Pi_0(q,\omega\,|\,\phi,\lambda_0)$ of $\alpha-\mathcal{T}_3$ lattices at $T=0$ K could substantially differ from that of graphene (red curves for $\phi=0$), as displayed in Fig. 1. This difference is attributed to additional channels for electron transitions resulting from the middle flat band, as depicted in the inset of Fig. 1(b), especially for $\hbar\omega$ close to the Fermi energy E_F.
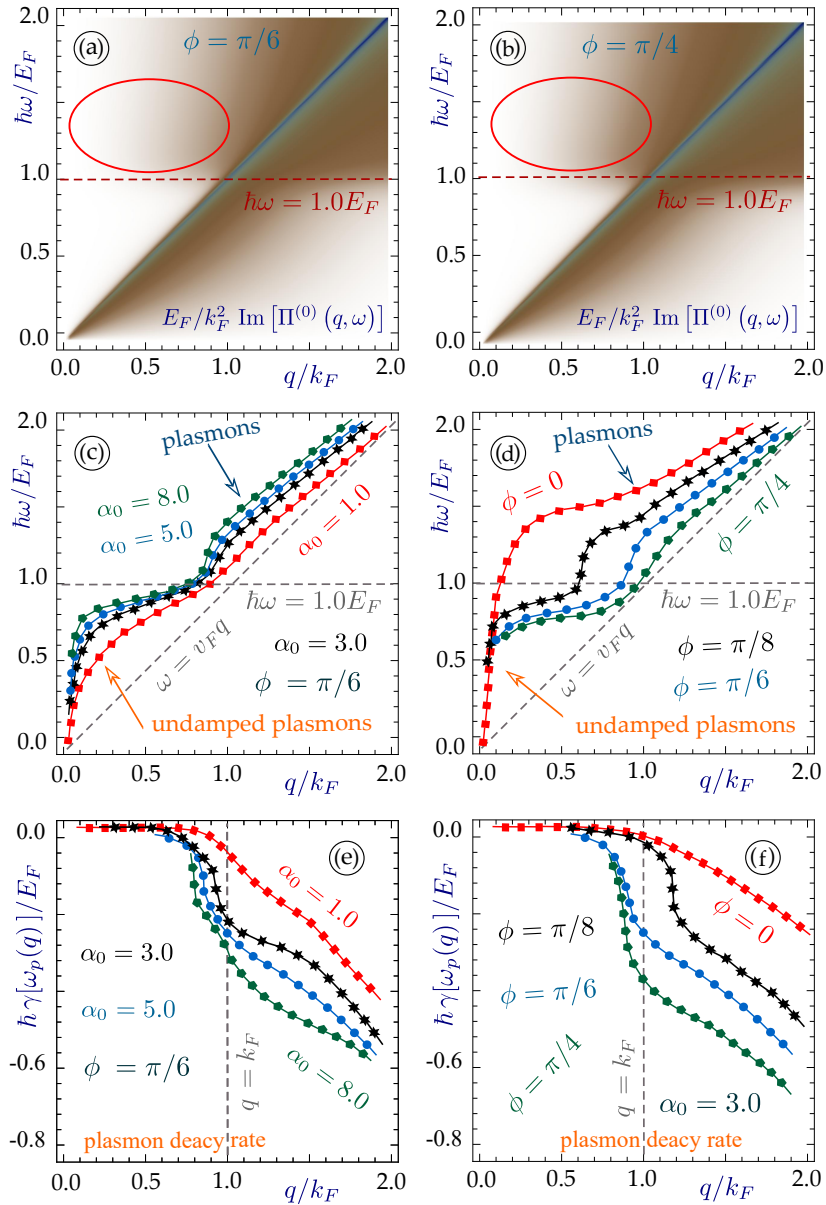
FIG. 2: (Color online) Plasmon damping regions [(a) $\phi = \pi/6$, (b) $\phi = \pi/4$] and plasmon branches [(c), (d)] for various types of $\alpha - \mathcal{T}_3$ lattices in the absence of external irradiation ($\lambda_0 = 0$). Two upper panels display $\text{Im}[\Pi^{(0)}(q, \omega \,|\, \phi)]$, which indicate regions for single-particle excitations. Here, two partially-damping regions above the $\hbar\omega = E_F$ line are highlighted by red circles. Panel (c) presents plasmon dispersions for fixed $\phi = \pi/6$ but different α_0 values, while panel (d) exhibits plasmon modes for fixed $\alpha_0 = 3.0$ and several phase values of ϕ. Plots (e) and (f) demonstrate the damping rates $\gamma[\omega_p(q)]$ of the plasmons shown at panels (c) and (d), correspondingly.

The complex $\Pi_0(q, \omega \,|\, \phi, \lambda_0 = 0)$ at $T = 0\,\text{K}$ for $0 \leq \alpha \leq 1$ (or $0 \leq \phi \leq \pi/4$) are presented in Figs. 1(a)−1(d). Its imaginary part for $q < k_F$ in Fig. 1(a) shows a noticeable peak at a lower $\hbar\omega$ in comparison with graphene (red curve). For $q > k_F$ in Fig. 1(b), however, there exists a singular pole scaled as $\backsim -1/\sqrt{|v_F^2 q^2 - \omega^2|}$. An accompanied zigzag feature in its real part can also be seen in Figs. 1(c) and 1(d), which reveals the q-dispersion of a plasmon mode.

Physically, the particle-hole continuum comprising the single-particle excitation regions are defined as the regions with $\text{Im}[\Pi_0(q, \omega \,|\, \phi, \lambda_0)] \neq 0$. Once a plasmon branch enters into such region, it will suffer from Landau damping resulting in the decay of a plasmon mode into single-particle excitations. Thus, we would concentrate on finding the regions of damping-free plasmon modes with $\text{Im}[\Pi_0(q, \omega \,|\, \phi, \lambda_0)] = 0$.

In our calculations, we look for a (q, ω) region in which plasmon modes could be present. In fact, we find that, for all $\alpha - \mathcal{T}_3$ materials, only one *triangle* region appears below the Fermi level E_F plus another one (indicated by a red

circle) above the main diagonal ($\omega = v_F q$), as shown in Figs. 2(a) and 2(b). Even though there are additional areas free from Landau damping for $q > 2k_F$, plasmon modes in free-standing 2D materials cannot exist there. Strictly speaking, a plasmon mode will decay once it goes above the line $\hbar\omega/E_F = 1$. Interestingly, the damping strength varies with ϕ and becomes infinitesimally small and even disappears for graphene with $\phi \to 0$.

The distortion of plasmon dispersions around $\hbar\omega \approx E_F$ in Fig. 2(c) reflects the contributions associated with electron transitions both starting from and ending in the flat band. The influence of this flat band amplifies itself close to the $\hbar\omega/E_F = 1$ line, where various plasmon branches, corresponding to different α_0 values, are expected to be pinched at a single crossing point intersected by the $\hbar\omega/E_F = 1$ line and diagonal to $\hbar\omega = \hbar v_F q$, as found for a dice lattice. [7] Here, however, we find these distorted plasmon branches with $\phi = \pi/6$ are separated from the diagonal $\hbar\omega = \hbar v_F q$ and only display two peaks below and above the $\hbar\omega/E_F = 1$ line instead of pinching. Moreover, various plasmon branches with different α_0 values will cross the $\hbar\omega/E_F = 1$ line at slightly different q values.

We find one interesting feature by analyzing the degree to which various plasmon modes with a fixed α_0 in Fig. 2(d) are away from the diagonal $\hbar\omega = \hbar v_F q$ for the boundary of single-particle excitations. For $\phi \neq 0$, the plasmon energy is always smaller than that of graphene ($\phi = 0$, red curve). For all finite ϕ, there exist two steps for plasmon energies, which are separated by the $\hbar\omega = E_F$ line, except for $\phi = 0$. The undamped first step under the $\hbar\omega/E_F = 1$ line spans a much larger (up to ten times) q range compared to graphene. For $q \ll E_F/(\hbar v_F)$, all plasmon modes become nearly degenerate, corresponding to the electron transitions across the Fermi energy within the upper Dirac cone. On the other hand, the electron transitions between the flat band and the upper Dirac cone are associated with the range around $q \approx E_F/(\hbar v_F)$ in Fig. 2(d). Furthermore, the electron transitions resulting from two Dirac cones relate to the $q \geq 2E_F/(\hbar v_F)$ range. In summary, we believe the best condition for observing the ϕ–dependence of plasmon dispersions and damping is around $\phi = 0$ because the results for $\phi = \pi/6$ and a dice lattice show only little difference in Fig. 2(d).

The nonlocal plasmon-decay rate $\gamma[q, \omega_p(q) \,|\, \phi]$, close to the plasmon frequency $\omega \approx \omega_p(q)$, can be approximately as [7, 56]

$$\gamma[q, \omega_p(q) \,|\, \phi] = \frac{\text{Im}\left[\Pi^{(0)}(q, \omega_p \,|\, \phi)\right]}{\text{Re}\left\{ \left. \dfrac{\partial \Pi^{(0)}(q, \omega \,|\, \phi)}{\partial \omega} \right|_{\omega = \omega_p} \right\}} \, , \tag{5}$$

where q is the wave number of plasmon mode and $\omega_p(q)$ represents the dispersion of plasmon energy. The plasmon mode becomes long lived and could be considered stable only outside of the particle-hole continuum, or within the Landau-damping-free regions where $\text{Im}\left[\Pi_0(q, \omega \,|\, \phi)\right] = 0$. The only damping-free region for $\alpha - \mathcal{T}_3$ is a triangle above the main diagonal $\omega > v_F q$ and below the Fermi level $\omega < E_F/\hbar$ at the same time. Plasmon excitations in all other regions could be strongly damped.

Our numerically calculated plasmon damping rates $\gamma[q, \omega_p(q) \,|\, \phi]$ are presented in Fig. 2 (e) and 2 (f). The magnitude of plasmon damping can be affected by three factors. The first and the foremost one is the nonzero $\text{Im}\left[\Pi^{(0)}(q, \omega_p \,|\, \phi)\right]$ or the numerator in Eq. (5), which determines whether the damping exists or not. $\gamma[q, \omega_p(q) \,|\, \phi]$ also depends on ω in $\text{Re}\left[\Pi^{(0)}(q, \omega \,|\, \phi)\right]$ or the denominator in Eq. (5). To excite a plasmon mode, we need $\text{Re}\left[\Pi^{(0)}(q, \omega \,|\, \phi)\right] > 0$, and meanwhile, we also require a steep change of it with respect to ω around $\omega = \omega_p(q)$ so as to reduce the decay rate in Eq. (5). Finally, the separation of the $\omega_p(q)$ region away from the damping region ensures a full damping-free plasmon mode.

Generally speaking, low-energy plasmon modes are free from damping since they locate below the Fermi level. Once they exceed the Fermi energy, these high-energy plasmon modes start suffering from the Landau damping. Although both the real and imaginary parts of $\Pi^{(0)}(q, \omega_p \,|\, \phi)$ do no not depend on α_0, $\omega_p(q)$ does depend on α_0, which strongly affects the damping of high-energy plasmon modes. Moreover, the phase ϕ can not only modify the real and imaginary parts of $\Pi^{(0)}(q, \omega_p \,|\, \phi)$, but also play a similar role as α_0 in controlling $\omega_p(q)$ for high-energy plasmon modes.

The feature with different values of $\phi = \tan^{-1}\alpha$, as shown in Fig. 2(f), looks very interesting since, for graphene and others with very small α, their plasmon damping starts at a frequency in the range of $E_F < \hbar\omega < 2E_F - \hbar v_F q$, much higher than the Fermi level. In fact, we find from Fig. 2(d) that the plasmon branches with $\alpha > 0$ reach the Fermi level at much larger q values in comparison with graphene. Therefore, either as $\omega_p(q)$ is higher for fixed q or as q is smaller for fixed $\hbar\omega_p(q) = E_F$, one finds much less damping for high-energy plasmon modes, and the damping becomes the lowest for graphene with $\alpha = 0$.

Next, we turn our attention to the plasmon dispersions of a dice lattice in the presence of a circularly-polarized laser field. The dice lattice ($\phi = \pi/4$) becomes the most different entity compared to graphene ($\phi = 0$), for the latter the effect of circularly-polarized light is simply adding a band gap (via a $\hat{\Sigma}_z^{(2)}$ term) to the bare Dirac Hamiltonian. [46, 56]
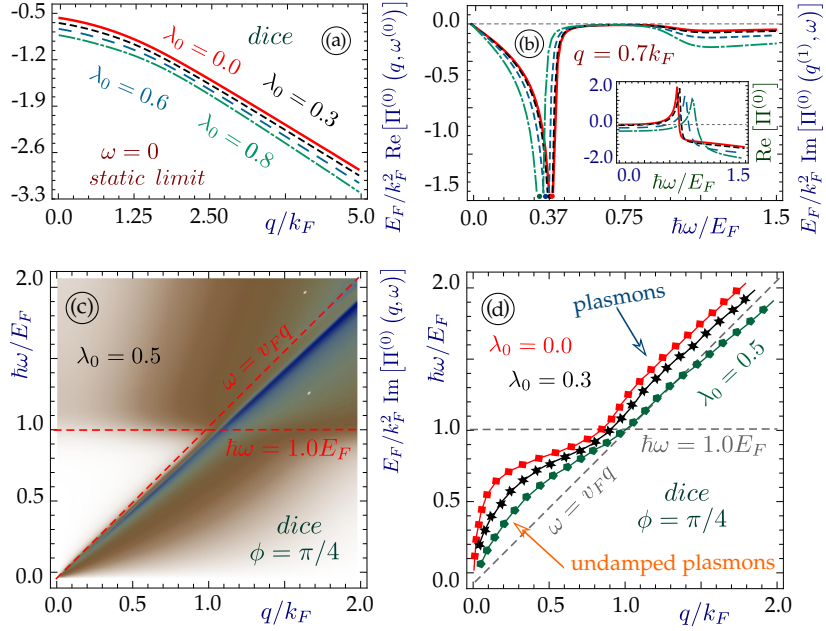
FIG. 3: (Color online) $\Pi_0(q,\omega\,|\,\lambda_0)$ in units of k_F^2/E_F [(a)-(c)] and plasmon dispersions (d) for a dice lattice ($\phi=\pi/4$) under a circularly-polarized laser field with various λ_0 values. Panel (a) shows the q dependence of Re$[\Pi_0(q,\omega=0\,|\,\lambda_0)]$ in the static limit $\omega=0$. Plot (b) presents the $\hbar\omega$ dependence of Im$[\Pi_0(q,\omega\,|\,\lambda_0)]$ at $q/k_F=0.7$, while its inset displays the $\hbar\omega$ dependence for Re$[\Pi_0(q,\omega\,|\,\lambda_0)]$. Plot (c) demonstrates the particle-hole modes Im$[\Pi_0(q,\omega\,|\,\phi,\lambda_0)]\neq0$ at $\lambda_0=0.5$.

The distinctive feature of a dice lattice is that Re$[\Pi_0(q,\omega=0\,|\,\lambda_0)]$ no loner becomes a constant within the region of $q<2\,k_F$, as demonstrated in Fig. 3(a). Furthermore, as λ_0 increases from zero, the negative peak of Im$[\Pi_0(q,\omega\,|\,\lambda_0)]$ shifts downwards in $\hbar\omega$, while the positive peak of Re$[\Pi_0(q,\omega\,|\,\lambda_0)]$ shifts upwards, as seen in Fig. 3(b) and its inset.

For an irradiated dice lattice, the region with the highest Landau damping is shifted downward below the main diagonal $\omega=v_Fq$, as found in Fig. 3(c). Once the dressing field is applied, the blue region expands towards lower frequencies due to the renormalization of two dispersive energy subbands. This feature is also seen in plasmon dispersions, as shown in Fig. 3(d). Starting from a $\smile\sqrt{q}$ dependence at low q, the graphene plasmon-dispersion, $\omega_p(q)$, later tends to follow the main diagonal resulting from the $1/q$ dependence in the 2D Coulomb potential. Consequently, a connection has been established between the expansion of blue region towards low frequency in Fig. 3(c) and the downward shift of $\omega_p(q)$ below the main diagonal in Fig. 3(d). This plasmon is obviously strongly damped and can not be considered stable.

The decrease of $\omega_p(q)$ of a dice lattice in the presence of circularly-polarized light is qualitatively similar to that of graphene, which is given by $\omega_p(q)\simeq\sqrt{q\,(1-\Delta_0^2/E_F^2)}$ in the long-wave limit due to opening a bandgap Δ_0 for graphene. In the current case, the peak in Re$[\Pi^{(0)}(q,\omega_p\,|\,\phi)]$ shifts with increasing irradiation power, accompanied by a shifting crossing point where Re$[\Pi^{(0)}(q,\omega_p\,|\,\phi)]$ changes its sign. The shift of a crossing point corresponds to continuously shaping of $\omega_p(q)$ with increasing laser intensity.

Although the laser field does not affect the undamped plasmon modes in the triangle region determined by $\omega>v_Fq$ and $\hbar\omega/E_F<1$, their dispersions are significantly modified beyond this triangle region above the diagonal, as presented in Fig. 3(d). Meanwhile, the plasmon energy decreases with increasing λ_0, similar to the single-electron dispersion in the presence of an energy gap. [56] However, no similarity to plasmon dispersions of graphene is found due to the addition of a middle flat band. It is worthwhile to mention that the plasmon branch extends into the region below the main diagonal for large λ_0 values.

As circularly polarized irradiation is applied, the energy subbands of a dice lattice vary in a way very different from that of graphene. The opened energy gap of the dice lattice is only a half of that of graphene, and becomes the lowest among all $\alpha-\mathcal{T}_3$ materials. Meanwhile, we find the Fermi velocity is renormalized at the same order as $\smile\lambda_0^4$ for the dice lattice, while the Fermi velocity in graphene remains unchanged [46].

For the plasmon damping in graphene, there exists a gap region between the interband and intraband single-particle excitation regimes. This gives rise to an "extended" undamped plasmon branch at higher energies and larger wave numbers. However, such a situation is invalid for an irradiated dice lattice because the damping region extends all over above the Fermi level.
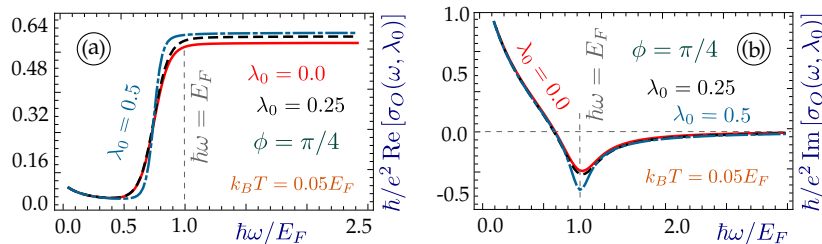
FIG. 4: (Color online) Real (a) and imaginary (b) parts of optical-current conductivity $\sigma_O(\omega\,|\,\lambda_0)$ in units of $e^2/\hbar$ for an irradiated dice lattice ($\phi = \pi/4$) as a function of $\hbar\omega$. Here, each curve corresponds to a specific λ_0 value for fixed ϕ and T.
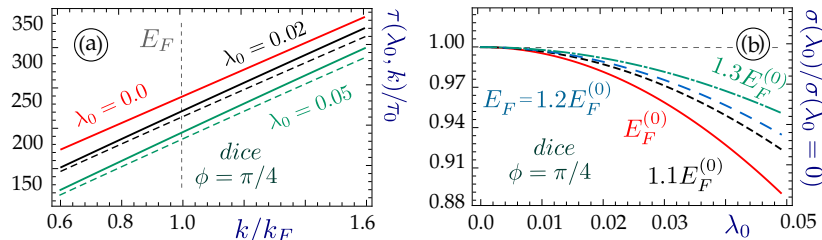

FIG. 5: (Color online) Transport conductivity $\sigma_T(\lambda_0)$ for an irradiated dice lattice. Panel (a) displays the relaxation time $\tau(k, \lambda_0)$ in units of $\tau_0 = 2\hbar E_F^{(0)}/(\pi n_i \alpha_0^2)$ as a function of wavevector k for various electron-light coupling constants λ_0 as labeled, where $E_F^{(0)}$ represents the Fermi energy for the case with $\mathcal{E}_0 = 0$. The dashed curves show the corresponding results without taking into account the laser-induced modification to the static dielectric function. Plot (b) presents the ratio $\sigma_T(\lambda_0)/\sigma_T(\lambda_0 = 0)$ as a function of λ_0 for different Fermi energies.

Finally, we would like to address the issue of laser-induced optical current. The result for the conductivity of a dissipative optical current can be obtained from the calculated complex polarization function $\Pi_0(q, \omega\,|\,\phi, \lambda_0)$. Specifically, the optical-current conductivity in the long-wavelength limit is given by $\sigma_O(\omega\,|\,\phi, \lambda_0) = \lim_{q\to 0}\left\{(ie^2\omega/q^2)\,\Pi_0(q, \omega\,|\,\phi, \lambda_0)\right\}$. [29] Consequently, the real part of $\sigma_O(\omega\,|\,\phi, \lambda_0)$ for optical current will correspond to the imaginary part of $\Pi_0(q, \omega\,|\,\phi, \lambda_0)$ for absorptive dissipation. On the other hand, the imaginary part of $\sigma_O(\omega\,|\,\phi, \lambda_0)$ will be associated with the real part of $\Pi_0(q, \omega\,|\,\phi, \lambda_0)$ for induced polarization.

Our numerical results for calculated optical-current conductivity in a dice lattice are presented in Fig. 4. Its real part $\mathrm{Re}\,[\sigma_O(\omega\,|\,\lambda_0)]$ presented in Fig. 4 (a) reveals that a high plateau starting nearly from $\hbar\omega = E_F$ extends well into a high-frequency region, and it is slightly enhanced by laser irradiation from the result $\simeq 1 + 4\lambda_0^2$ for graphene. [67, 68] This is in correspondence with an appearance of Landau damping for plasmon modes in the $q \to 0$ limit, as displayed in Fig. 3(c). In addition, for the imaginary part $\mathrm{Im}\,[\sigma_O(\omega\,|\,\lambda_0)]$, we find it independent of λ_0 except for $\hbar\omega$ close to E_F. The boundary position of nonzero $\mathrm{Re}\,[\sigma_O(\omega)]$ is not affected by irradiation, similarly to the corresponding result for silicene [67]. The near-zero $\mathrm{Re}\,[\sigma_O(\omega)]$ below the Fermi energy E_F, on the other hand, can be attributed to state-blocking effect.

Furthermore, a negative peak in $\mathrm{Im}\,[\sigma_O(\omega\,|\,\lambda_0)]$ shows up at $\hbar\omega = E_F$ and becomes sharpened by increasing λ_0 due to laser irradiation. $\mathrm{Im}\,[\sigma_O(\omega\,|\,\lambda_0)]$ in the region of $\hbar\omega > 2E_F$ is fully suppressed to zero in the long-wavelength limit $q \to 0$. This is related to the fact that plasmon modes, determined by $\mathrm{Re}\,[\Pi_0(q, \omega\,|\,\lambda_0)] = q/2\pi\alpha_0$, do not exist in this region as $q \to 0$, as can be verified from Fig. 3(d). The magnitude of $\mathrm{Im}\,[\sigma_O(\omega)]$ for $\hbar\omega > E_F$ is mainly determined by the bandgap, and therefore, can be varied by the dressing field.

Here, we emphasize again that we limit our consideration only to low laser intensities, i.e., $\lambda_0 = (c_0/\hbar\omega) < 1$. Consequently, our previous model on derivation of the single electronic states remains valid and we can further identify physical effects from our analytical expressions in the lowest-order approximation.

IV. IMPURITY SCATTERING AND CONDUCTION CURRENT

In order to consider the transport conductivity of an irradiated dice lattice, we calculate $\sigma_T(\lambda_0)$ in the relaxation-time approximation, while the scattering potential is assumed as the point-like Coulomb interaction $U_{im}(r) = Z^*e/(4\pi\epsilon_0\epsilon_r r)$ with an impurity charge number Z^*. For finite electron doping $E_F > 0$, the inverse relaxation time is given by [69–72]

$$\frac{1}{\tau(k,\lambda_0)} = \frac{n_i}{2\pi\hbar} \int_0^{2\pi} d\beta_{\mathbf{k},\mathbf{k}'} \left(1 - \cos\beta_{\mathbf{k},\mathbf{k}'}\right)$$

$$\times \sum_{\tau=\pm 1} \int_0^\infty \frac{k'dk'}{|\epsilon(|\mathbf{k}-\mathbf{k}'|,\omega=0)|^2} \left| \int d^2\mathbf{r}\, \Phi_\gamma^\tau(\mathbf{r},\mathbf{k}',\lambda_0)\, U_{im}(r)\, \Phi_\gamma^\tau(\mathbf{r},\mathbf{k},\lambda_0) \right|^2 \delta[\varepsilon_\gamma(k,\lambda_0) - \varepsilon_\gamma(k',\lambda_0)]\,, \quad (6)$$

where $\gamma = +$, n_i represents the impurity areal density, $\beta_{\mathbf{k},\mathbf{k}'}$ is the angle between electron wavevectors $\mathbf{k}$ and $\mathbf{k}'$, the full electron wave function is $\Phi_\gamma^\tau(\mathbf{r},\mathbf{k},\lambda_0) = \Psi_\gamma^\tau(\mathbf{k},\lambda_0)\exp(i\mathbf{k}\cdot\mathbf{r})$. For isotropic band dispersions and electronic states, corresponding to circularly-polarized laser irradiation, the relaxation time, $\tau(k,\lambda_0)$, depends only on $k = |\mathbf{k}|$. In the absence of static screening, $\tau(k,\lambda_0)$ could be obtained analytically (see Appendix C).

For the isotropic case of circularly-polarized irradiation and at low temperatures, the electric-current J_0 per length under an applied DC electric field E_0 is expressed as (see Appendix C)

$$J_0 = \left(\frac{e}{\pi}\right)^2 E_0 \int d^2\mathbf{k}\, [v_\gamma(k,\lambda_0)]^2\, \tau(k,\lambda_0)\, \delta[\varepsilon_\gamma(k,\lambda_0) - E_F]\,, \quad (7)$$

where $v_\gamma(k,\lambda_0) = (1/\hbar)\,\partial\varepsilon_\gamma(k,\lambda_0)/\partial k$ is the electron group velocity.

The inverse relaxation time $1/\tau_0(k)$ for a non-irradiated dice lattice is $3/4$ times of that of graphene due to the change of wave-function overlap factors, which for graphene is equal to $(1+\cos\beta_{\mathbf{k},\mathbf{k}'})^2/4$. Dice lattice and graphene represent two limiting cases of $\alpha-\mathcal{T}_3$ lattices, and their $\tau_0(k)$ has already been calculated.[66] Once the circularly-polarized laser is applied, the ratio of inverse relaxation times becomes $\tau_0(k)/\tau(k,\lambda_0) \simeq 3\pi/4 - 7\pi/16\,\xi^2 + \cdots$, where $\xi = c_0\lambda_0/E_F = (e\mathcal{E}_0/\hbar\omega)^2(v_F/\omega k_F)$. This apparently leads to a substantial drop of $\sigma_T(\lambda_0)$ in the presence of a laser field $\mathcal{E}_0$. The exact ratio is predetermined by a pseudospin-1 wave function with three inequivalent components, and is not valid for graphene or a $2D$ electron gas.

Another factor for laser-induced reduction of $\sigma_T(\lambda_0)$ comes from the decreased electron group velocity $v_\gamma(k,\lambda_0)$. From Eq. (1), we find $[v_F(\lambda_0)]^2 \simeq v_F^2\left(1-\lambda_0^2/4\right)^2\left[1-(\lambda_0^2/4)\,(c_0/E_F)^2\right]$. Here, the two terms are related to the variation of the Fermi velocity v_F and the opening of a bandgap $E_G = \lambda_0 c_0$, respectively. Both of these effects lead to a decrease in $\sigma_T(\lambda_0)$ with λ_0. Using $\mathbb{I}_0 = 10\,W/cm^2$ and $c_0/E_F \simeq 9.75$, we find the magnitude of the second term is much larger than the first term. Besides, the screening factor is also reduced in the presence of a laser field which must be taken into account for an accurate determination of $\sigma_T(\lambda_0)$.

The above obtained results for a dice lattice are quite different from those of graphene. For graphene, we get $[v_F(\lambda_0)]^2/v_F^2 \backsim 1 - \lambda_0^2\,(c_0/E_F)^2$, and then, the inverse relaxation time $\tau_0/\tau(k,\lambda_0) \backsim 1 - 3\lambda_0^2\,(c_0/E_F)^2$,[55] as well as the reduced transport conductivity $\sigma_T(\lambda_0)/\sigma_T(\lambda_0 = 0) \backsim 1 - 4\lambda_0^2\,(c_0/E_F)^2$.

Numerical results for the relaxation-time $\tau(k,\lambda_0)/\tau_0$ and the transport-conductivity $\sigma_T(\lambda_0)/\sigma_T(\lambda_0 = 0)$ in a dice lattice are presented in Fig. 5, including the laser-induced modification to the static screening for elastic scattering between electrons and impurities. From Fig. 5(a), we find the relaxation time $\tau(k,\lambda_0)$ is approximately proportional to k and decreases with increasing λ_0. Moreover, the laser-induced modification (dashed curves) to the static dielectric function is important quantitatively. From Fig. 5(b), we know the transport conductivity $\sigma_T(\lambda_0)$ decreases with λ_0 nonlinearly compared to the result in the absence of a laser field, which agrees with our analytical evaluations. In addition, for fixed λ_0 this reduction effect becomes less and less significant with increasing Fermi energy since the correction is proportional to c_0/E_F.

V. CONCLUDING REMARKS AND SUMMARY

In this paper, we have calculated and analyzed numerical results for plasmon-mode dispersion and damping as well as their effects on displacement and transport currents of electrons in irradiated $\alpha-\mathcal{T}_3$ materials by a circularly-polarized laser. As a result, we conclude that the intensity of a laser field can be used effectively to control both optical and transport conductivities in the system, in addition to a tuning of them with a structure parameter $0 < \alpha \leq 1$ for different $\alpha-\mathcal{T}_3$ lattices.

The plasmon dispersions, their damping, optical and Boltzmann conductivities of pseudospin-1 $\alpha-\mathcal{T}_3$ materials are very different from those of pesudospin-1/2 graphene. A physical explanation of that is the existence of a topological

flat band and associated topological properties of the electronic states. The flat band stays dispersionless in the presence of the dressing field, while the dispersions of symmetrical valence and conduction bands change due to both opened energy bandgap and reduction of Fermi velocity. This unique feature for pseudospin-1 $\alpha - \mathcal{T}_3$ materials is in a stark contrast to laser-renormalization behavior in graphene where the only the energy gap plays a role.

In particular, for the whole range of α values, we observe that the tuning of plasmon modes reaches the strongest as $\phi \backsim 0$ on the graphene side, but it becomes relatively weak as $\phi \backsim \pi/4$ on the dice-lattice side. Meanwhile, a significant increase in the plasmon damping above the Fermi level, accompanied by a change of plasmon dispersion below the Fermi energy, is found with increasing α from zero to one. Moreover, the pinching of plasmon dispersion around the Fermi energy also shows up, which can be attributed to electron transitions from the middle flat band to the upper Dirac cone.

After a circularly-polarized laser has been applied to a dice lattice, the plasmon mode is modified dramatically by lowering its dispersion curve below the main diagonal. Meanwhile, the transport conductivity of electrons in a dice lattice decreases with increasing laser intensity. These results indicate that electron dynamics under irradiation in graphene is quite different from that in a dice lattice and can be controlled by laser, which further implies that such a difference can be tuned by a structure parameter α for $\alpha - \mathcal{T}_3$ materials. All of these are expected to provide very useful information and guidance for designing nano-electronic and nano-plasmonic devices based on innovative low-dimensional $\alpha - \mathcal{T}_3$ materials.

Appendix A: Laser-Renormalized Electronic States

The low-energy Hamiltonian for a dice lattice irradiated by a laser field under the off-resonance condition can be obtained from a perturbation theory by using the Floquet-Magnus expansion [58], given by

$$\mathbb{H}_\tau(k \,|\, \theta_{\mathbf{k}}) = -\tau\lambda_0\,\frac{c_0}{2}\,\hat{\Sigma}_z + \frac{\hbar}{\sqrt{2}}\,\mathcal{V}_F(\lambda_0) \sum_{s=\pm} \hat{\Sigma}_s\, k_\tau^s \,, \tag{A1}$$

where $c_0 = e\,\mathcal{E}_0 v_F/\omega$ is the interaction energy, $\lambda_0 = c_0/(\hbar\omega)$ is a small dimensionless light-electron coupling constant used for the expansion, $\mathcal{V}_F(\lambda_0) = \left[1 - (\lambda_0/2)^2\right] v_F$ is the renormalized Fermi velocity, $k_\tau^\pm = \tau k_x \pm i k_y = \tau k\, e^{i\tau\theta_{\mathbf{k}}}$, and $\theta_{\mathbf{k}} = \tan^{-1}(k_y/k_x)$. Additionally, $\hat{\Sigma}_\pm = \hat{\Sigma}_x \pm i\hat{\Sigma}_y$, where $\hat{\Sigma}_{x,y,z}$ are 3×3 Pauli matrices defined in Ref. [58].

Energy dispersions of the electron dressed states associated with the Hamiltonian in Eq. (A1) are found for $\gamma = \pm$ to be

$$\varepsilon_0(k,\lambda_0) = 0 \quad \text{and} \tag{A2}$$

$$\varepsilon_\gamma(k,\lambda_0) = \gamma \left\{ (\hbar v_F k)^2 \left[1 - \left(\frac{\lambda_0}{2}\right)^2\right]^2 + c_0^2 \left(\frac{\lambda_0}{2}\right)^2 \right\}^{1/2} .$$

This gives rise to an energy bandgap $E_G = \lambda_0 c_0 \equiv 2\Delta_0$ which is exactly one half the graphene bandgap under the same irradiation, while renormalized Fermi velocity stays the same as that of graphene. Clearly, the obtained dispersions do not depend on the valley index $\tau = \pm 1$.

Furthermore, the electron wave functions for an irradiated dice lattice are calculated as

$$\Psi_\gamma^\tau(\boldsymbol{k},\lambda_0) = \frac{1}{\sqrt{\mathcal{N}_\gamma^\tau}} \begin{bmatrix} \tau\, \mathcal{C}_{1,\gamma}^\tau\, e^{-i\tau\theta_{\mathbf{k}}} \\ \mathcal{C}_{2,\gamma}^\tau \\ \tau\,(\hbar v_F k)^2\, e^{+i\tau\theta_{\mathbf{k}}} \end{bmatrix} , \tag{A3}$$

where

$$\mathcal{C}_{1,\gamma}^{\tau}(k,\lambda_0) = (\hbar v_F k)^2 + 2\left(\delta_\lambda^2 - \gamma\tau\delta_\lambda\sqrt{(\hbar v_F k)^2 + \delta_\lambda^2}\right) \,, \tag{A4}$$

$$\mathcal{C}_{2,\gamma}^{\tau}(k,\lambda_0) = \sqrt{2}\,\gamma\,(\hbar v_F k)\left(\sqrt{(\hbar v_F k)^2 + \delta_\lambda^2} - \gamma\tau\delta_\lambda\right) \,,$$

$$\mathcal{N}_\gamma^\tau(k,\lambda_0 \ll 1) \simeq 4(\hbar v_F k)^4 - 4\gamma\tau\,c_0\lambda_0\,(\hbar v_F k)^3 + 3\left[c_0\lambda_0\,(\hbar v_F k)\right]^2 + \dots \,.$$

Here, our parameter $\delta_\lambda = 2\lambda_0\,c_0/(4 - \lambda_0^2)$ is different from the energy gap $E_G = \lambda_0 c_0 = 2\Delta_0$. For $\gamma = +1$, the wave function in Eq. (A3) for the conduction band, can be simply rewritten as

$$\Psi_\gamma^\tau(\boldsymbol{k},\lambda_0) = \begin{bmatrix} \tau\,c_1^{(+1)}\,e^{-i\tau\theta_{\mathbf{k}}} \\ c_2^{(+1)} \\ \tau\,c_3^{(+1)}\,e^{+i\tau\theta_{\mathbf{k}}} \end{bmatrix} \,, \tag{A5}$$

where

$$c_1^{(+1)} = \frac{\mathcal{C}_{1,\gamma=1}^{\tau}}{\sqrt{\mathcal{N}_{\gamma=1}^{\tau}}} \,, \qquad \left(c_1^{(+1)}\right)^2 \simeq \frac{1}{4} - \frac{\lambda_0}{4}\frac{c_0}{\hbar v_F k}\tau + \frac{\lambda_0^2}{16}\left(\frac{c_0}{\hbar v_F k}\right)^2 \dots \,, \tag{A6}$$

$$c_2^{(+1)} = \frac{\mathcal{C}_{2,\gamma=1}^{\tau}}{\sqrt{\mathcal{N}_{\gamma=1}^{\tau}}} \,, \qquad \left(c_2^{(+1)}\right)^2 \simeq \frac{1}{2} - \frac{\lambda_0^2}{8}\left(\frac{c_0}{\hbar v_F k}\right)^2 + \dots \,,$$

$$c_3^{(+1)} = \frac{(\hbar v_F k)^2}{\sqrt{\mathcal{N}_{\gamma=1}^{\tau}}} \,, \qquad \left(c_3^{(+1)}\right)^2 \simeq \frac{1}{4} + \frac{\lambda_0}{4}\frac{c_0}{\hbar v_F k}\tau + \frac{\lambda_0^2}{16}\left(\frac{c_0}{\hbar v_F k}\right)^2 + \dots \,.$$

For the flat band, on the other hand, we obtain

$$\Psi_0^\tau(\boldsymbol{k},\lambda_0) = \frac{1}{\sqrt{\mathcal{N}_{\gamma=0}^{\tau}}}\begin{bmatrix} \hbar v_F k\,e^{-i\tau\theta_{\mathbf{k}}} \\ 2\sqrt{2}\,c_0\lambda_0/(4 - \lambda_0^2) \\ -\hbar v_F k\,e^{+i\tau\theta_{\mathbf{k}}} \end{bmatrix} \,, \tag{A7}$$

where

$$\mathcal{N}_{\gamma=0}^{\tau}(k,\lambda_0 \ll 1) \simeq 2(\hbar v_F k)^2 + \frac{1}{2}\,(\lambda_0 c_0)^2 + \dots \,. \tag{A8}$$

Here, the wave-function components are no longer equal to each other, as expected for a finite energy gap.

The obtained wave function (A7) could be rewritten as

$$\Psi_0^\tau(\boldsymbol{k},\lambda_0) = \begin{bmatrix} c_1^{(0)}\,e^{-i\tau\theta_{\mathbf{k}}} \\ c_2^{(0)} \\ -c_1^{(0)}\,e^{+i\tau\theta_{\mathbf{k}}} \end{bmatrix} \,, \tag{A9}$$

where

$$c_1^{(0)} = \frac{\hbar v_F k}{\sqrt{\mathcal{N}_0}} \,, \qquad \left(c_1^{(0)}\right)^2 \simeq \frac{1}{2} - \frac{1}{8}\left(\frac{\lambda_0 c_0}{\hbar v_F k}\right)^2 + \dots \,, \tag{A10}$$

$$c_2^{(0)} = \frac{2\sqrt{2}\lambda_0}{4 - \lambda_0^2}\frac{c_0}{\sqrt{\mathcal{N}_0}} \,, \qquad \left(c_2^{(0)}\right)^2 \simeq \frac{1}{4}\left(\frac{\lambda_0 c_0}{\hbar v_F k}\right)^2 + \dots \,.$$

Here, it is important to notice that the laser-induced corrections to the flat band wave function do not depend on the valley index τ in contrast to the cases with $\gamma = \pm 1$.

Appendix B: Wave-Function Overlap

The prefactor, or the overlap of two electronic states, is defined by a scalar product $\mathbb{O}_{\gamma,\gamma'}^{\tau}(\boldsymbol{k}, \boldsymbol{k}' \,|\, \phi, \lambda_0)$ of the initial $\Psi_{\gamma}^{\tau}(\boldsymbol{k}, \lambda_0)$ and scattered $\Psi_{\gamma'}^{\tau}(\boldsymbol{k}', \lambda_0)$ electronic states with the wave vectors $\boldsymbol{k}$ and $\boldsymbol{k}' = \boldsymbol{k} + \boldsymbol{q}$

$$\mathbb{O}_{\gamma,\gamma'}^{\tau}(\boldsymbol{k}, \boldsymbol{k} + \boldsymbol{q} \,|\, \phi, \lambda_0) = \left| \mathbb{S}_{\gamma,\gamma'}^{\tau}(\boldsymbol{k}, \boldsymbol{k} + \boldsymbol{q} \,|\, \phi, \lambda_0) \right|^2 , \tag{B1}$$

$$\mathbb{S}_{\gamma,\gamma'}^{\tau}(\boldsymbol{k}, \boldsymbol{k} + \boldsymbol{q} \,|\, \phi, \lambda_0) = \left\langle \, \Psi_{\gamma}^{\tau}(\boldsymbol{k}, \lambda_0) \,\middle|\, \Psi_{\gamma'}^{\tau}(\boldsymbol{k} + \boldsymbol{q}, \lambda_0) \, \right\rangle ,$$

where $k' = \sqrt{k^2 + q^2 + 2kq\cos\beta_{\mathbf{k},\mathbf{k}'}}$ and $\beta_{\mathbf{k},\mathbf{k}'} = \theta_{\mathbf{k}'} - \theta_{\mathbf{k}}$.

For an irradiated ($\lambda_0 > 0$) dice lattice with $\phi = \pi/4$ and $\tau = +1$, we obtain

$$\mathbb{S}_{0,+1}(\boldsymbol{k}, \boldsymbol{k}' \,|\, \phi = \pi/4, \lambda_0) = c_1^{(0)}(k)\, c_1^{(+1)}(k')\, \mathrm{e}^{-i\tau\beta_{\mathbf{k},\mathbf{k}'}} + c_2^{(0)}(k)\, c_2^{(+1)}(k') - c_1^{(0)}(k)\, c_3^{(+1)}(k') \mathrm{e}^{+i\tau\beta_{\mathbf{k},\mathbf{k}'}} , \tag{B2}$$

which corresponds to the transitions from the flat band $\gamma = 0$ to the conduction band with $\gamma' = +1$, ($0 \leftrightarrow +1$ and back. Similarly, we have

$$\mathbb{S}_{-1,+1}(\boldsymbol{k}, \boldsymbol{k}' \,|\, \phi = \pi/4, \lambda_0) = c_1^{(-1)}(k)\, c_1^{(+1)}(k')\, \mathrm{e}^{-i\tau\beta_{\mathbf{k},\mathbf{k}'}} + c_2^{(-1)}(k)\, c_2^{(+1)}(k') + c_3^{(-1)}(k)\, c_3^{(+1)}(k')\, \mathrm{e}^{+i\tau\beta_{\mathbf{k},\mathbf{k}'}} \tag{B3}$$

for the transitions between the valence $\gamma = -1$ and conduction band with $\gamma' = +1$, ($-1 \leftrightarrow +1$), and finally,

$$\mathbb{S}_{+1,+1}(\boldsymbol{k}, \boldsymbol{k}' \,|\, \phi = \pi/4, \lambda_0) = c_1^{(+1)}(k)\, c_1^{(+1)}(k')\, \mathrm{e}^{-i\tau\beta_{\mathbf{k},\mathbf{k}'}} + c_2^{(+1)}(k)\, c_2^{(+1)}(k') + c_3^{(+1)}(k)\, c_3^{(+1)}(k')\, \mathrm{e}^{+i\tau\beta_{\mathbf{k},\mathbf{k}'}} . \tag{B4}$$

We exclude the remaining possible transitions $-1 \leftrightarrow -1$ inside the valence band and between the flat and valences bands $0 \leftrightarrow -1$, which are inactive at zero temperature for electron doping ($E_F > 0$). In the absence of irradiation ($\lambda_0 = 0$), these three overlap factors are given in Table C.

Appendix C: Laser-Renormalized Electron Transport

For a finite electron doping $E_F > 0$, the inverse relaxation time is calculated as

$$\frac{1}{\tau(k, \lambda_0)} = \frac{n_i}{2\pi\hbar} \int_0^{2\pi} d\beta_{\mathbf{k},\mathbf{k}'} (1 - \cos\beta_{\mathbf{k},\mathbf{k}'})$$

$$\times \sum_{\tau=\pm 1} \int_0^{\infty} \frac{k'dk'}{\left| \epsilon(\boldsymbol{k} - \boldsymbol{k}'|, \omega = 0) \right|^2} \left| \int d^2\boldsymbol{r}\, \Phi_{\gamma}^{\tau}(\boldsymbol{r}, \boldsymbol{k}', \lambda_0)\, U_{im}(r)\, \Phi_{\gamma}^{\tau}(\boldsymbol{r}, \boldsymbol{k}, \lambda_0) \right|^2 \delta[\varepsilon_{\gamma}(k, \lambda_0) - \varepsilon_{\gamma}(k', \lambda_0)] , \tag{C1}$$

where $\beta_{\mathbf{k},\mathbf{k}'}$ is the angle between $\boldsymbol{k}$ and $\boldsymbol{k}'$, the complete wave function is $\Phi_{\gamma}^{\tau}(\boldsymbol{r}, \boldsymbol{k}, \lambda_0) = \Psi_{\gamma}^{\tau}(\boldsymbol{r}, \boldsymbol{k}, \lambda_0) \exp(i\,\boldsymbol{k} \cdot \boldsymbol{r})$, and $\gamma = +1$. For isotropic dispersions and electronic states, corresponding to the circularly-polarized irradiation, the relaxation time depends only on $k = |\boldsymbol{k}|$.

In our analytical evaluation, we neglect the static-screening factor $1/|\epsilon(q, \omega = 0)|^2$ in Eq. (C1). Since we concentrate on the ratio of two inverse relaxation times with/without irradiation, we expect only the change in static dielectric function with λ_0 will be ignored. We begin with the scattering potential matrix element in Eq. (C1), given by

$$\mathbb{W}_{\gamma}^{\tau}(\boldsymbol{k}, \boldsymbol{k}') = \int d^2\boldsymbol{r}\, \Phi_{\gamma}^{\tau}(\boldsymbol{r}, \boldsymbol{k}', \lambda_0)\, U_{im}(r)\, \Phi_{\gamma}^{\tau}(\boldsymbol{r}, \boldsymbol{k}, \lambda_0) , \tag{C2}$$

where $U_{im}(r) = e^2/(4\pi\epsilon_0\epsilon_r r) \equiv \alpha_0/r$. As a result, we get

$$\mathbb{W}_{\gamma}^{\tau}(\boldsymbol{k}, \boldsymbol{k}') = \alpha_0\, \mathbb{S}_{\gamma,\gamma}^{\tau}(\boldsymbol{k}, \boldsymbol{k}' \,|\, \phi, \lambda_0) \int \frac{d^2\boldsymbol{r}}{r} \exp\left[i(\boldsymbol{k} - \boldsymbol{k}') \cdot \boldsymbol{r} \right] \equiv U_0(|\boldsymbol{k} - \boldsymbol{k}'|)\, \mathbb{S}_{\gamma,\gamma}^{\tau}(\boldsymbol{k}, \boldsymbol{k}' \,|\, \phi, \lambda_0) , \tag{C3}$$

Material	Overlap	Inverse relaxation time
Graphene	$(1 + \cos \beta_{\mathbf{k},\mathbf{k}'})/2$	π
Dice lattice	$(1 + \cos \beta_{\mathbf{k},\mathbf{k}'})^2/4$	$3\pi/4$
$\alpha - \mathcal{T}_3$	$(1/4)\left[(1 + \cos \beta_{\mathbf{k},\mathbf{k}'})^2 + \cos^2(2\phi)\sin^2 \beta_{\mathbf{k},\mathbf{k}'}\right]$	$(\pi/8)\left[7 + \cos(4\phi)\right]$

TABLE I: Prefactors (wave-function overlaps), and inverse relaxation time $\mathbb{I}(k)$ factor from Eq. (C8) for graphene and general $\alpha - \mathcal{T}_3$ materials in the absence of external irradiation ($\lambda_0 = 0$).

where $\mathbb{S}_{\gamma,\gamma}^{\tau}(\boldsymbol{k}, \boldsymbol{k}' \,|\, \phi, \lambda_0)$ is defined in Eq. (B1) and

$$U_0(q) = \alpha_0 \int d^2\boldsymbol{r} \, \frac{\exp(i\boldsymbol{q} \cdot \boldsymbol{r})}{r} = \frac{2\pi\alpha_0}{q} \,. \tag{C4}$$

The transition rate in the Born approximation is written as

$$\mathbb{T}_{\gamma}^{\tau}(\boldsymbol{k}, \boldsymbol{k}') = \frac{2\pi}{\hbar} \left| \mathbb{W}_{\gamma}^{\tau}(\boldsymbol{k}, \boldsymbol{k}') \right|^2 \delta[\varepsilon_{\gamma}(k, \lambda_0) - \varepsilon_{\gamma}(k', \lambda_0)] \,, \tag{C5}$$

where

$$\delta[\varepsilon_{\gamma}(k, \lambda_0) - \varepsilon_{\gamma}(k', \lambda_0)] = \frac{\delta(k - k')}{\hbar v_F} \,, \tag{C6}$$

$$|\boldsymbol{k} - \boldsymbol{k}'| = 2k \sin\left(\frac{\beta_{\mathbf{k},\mathbf{k}'}}{2}\right) \,.$$

By using the result in Eq. (C5), the inverse relaxation time can be formally written as

$$\frac{1}{\tau_{\gamma}(k, \lambda_0)} = \sum_{\tau = \pm 1} \frac{n_i}{(2\pi)^2} \int_0^{2\pi} d\beta_{\mathbf{k},\mathbf{k}'} \left(1 - \cos \beta_{\mathbf{k},\mathbf{k}'}\right) \int_0^{\infty} k' dk' \, \mathbb{T}_{\gamma}^{\tau}(\boldsymbol{k}, \boldsymbol{k}')\Big|_{k'=k} \,. \tag{C7}$$

Specifically, for $\gamma = +1$ we find

$$\frac{1}{\tau(k, \lambda_0)} = \frac{\pi n_i}{2 v_F} \left(\frac{\alpha_0}{\hbar}\right)^2 \frac{1}{k} \, \mathbb{I}(k, \lambda_0) \,, \tag{C8}$$

$$\mathbb{I}(k, \lambda_0) = \int_0^{2\pi} d\beta_{\mathbf{k},\mathbf{k}'} \left(\left\{ \left[\left(c_1^{(+1)}(k, \lambda_0)\right)^2 + \left(c_3^{(+1)}(k, \lambda_0)\right)^2 \right] \cos \beta_{\mathbf{k},\mathbf{k}'} + \left(c_2^{(+1)}(k, \lambda_0)\right)^2 \right\}^2 \right.$$

$$\left. + \left\{ \left[\left(c_1^{(+1)}(k, \lambda_0)\right)^2 - \left(c_3^{(+1)}(k, \lambda_0)\right)^2 \right] \sin \beta_{\mathbf{k},\mathbf{k}'} \right\}^2 \right) \,.$$

Finally, by using the relaxation-time approximation, the electric current $\boldsymbol{J}_0$ per length is calculated as

$$\boldsymbol{J}_0 = \left(\frac{e}{\pi}\right)^2 \int d^2\boldsymbol{k} \, \tau(k, \lambda_0) \, \boldsymbol{v}(\boldsymbol{k}) \left[\boldsymbol{E}_0 \cdot \boldsymbol{v}(\boldsymbol{k})\right] \left[-\frac{\partial f_0[\varepsilon(k, \lambda_0) - \mu_0]}{\partial \varepsilon(k, \lambda_0)}\right] \,, \tag{C9}$$

where $\boldsymbol{E}_0$ represents the external DC electric field, $\boldsymbol{v}(\boldsymbol{k}) = (1/\hbar)\,\partial\varepsilon(k, \lambda_0)/\partial\boldsymbol{k}$ is the group velocity of electrons, $f_0[\varepsilon(k, \lambda_0) - \mu_0] = \{1 + \exp[(\varepsilon(k, \lambda_0) - \mu_0)/k_B T]\}^{-1}$ is the thermal-equilibrium distribution function for electrons, μ_0 is the chemical potential, and T is the system temperature. If $T = 0\,\mathrm{K}$, we simply have $\partial f_0[\varepsilon(k, \lambda_0) - \mu_0]/\partial\varepsilon(k, \lambda_0) = \delta[\varepsilon(k, \lambda_0) - E_F]$ with Fermi energy E_F and the integral in Eq. (C9) can be performed analytically.

---

[1] A. Raoux, M. Morigi, J.-N. Fuchs, F. Piéchon, and G. Montambaux, Physical review letters **112**, 026402 (2014).

[2] J. Vidal, R. Mosseri, and B. Douçot, Physical review letters **81**, 5888 (1998).

[3] M. Vigh, L. Oroszlány, S. Vajna, P. San-Jose, G. Dávid, J. Cserti, and B. Dóra, Physical Review B **88**, 161413 (2013).

[4] M. Rizzi, V. Cataudella, and R. Fazio, Physical Review B **73**, 144511 (2006).

[5] K. Novoselov, A. K. Geim, S. Morozov, D. Jiang, M. Katsnelson, I. Grigorieva, S. Dubonos, and A. Firsov, nature **438**, 197 (2005).

[6] D. Leykam, A. Andreanov, and S. Flach, Advances in Physics: X **3**, 1473052 (2018).

[7] J. D. Malcolm and E. J. Nicol, Physical Review B **93**, 165433 (2016).

[8] J. Romhányi, K. Penc, and R. Ganesh, Nature communications **6**, 6805 (2015).

[9] W.-X. Qiu, S. Li, J.-H. Gao, Y. Zhou, and F.-C. Zhang, Physical Review B **94**, 241409 (2016).

[10] L. Santos, M. Baranov, J. I. Cirac, H.-U. Everts, H. Fehrmann, and M. Lewenstein, Physical review letters **93**, 030601 (2004).

[11] J. Ruostekoski, Physical review letters **103**, 080406 (2009).

[12] G.-B. Jo, J. Guzman, C. K. Thomas, P. Hosur, A. Vishwanath, and D. M. Stamper-Kurn, Physical review letters **108**, 045305 (2012).

[13] T. Baba, Nature photonics **2**, 465 (2008).

[14] X. Huang, Y. Lai, Z. H. Hang, H. Zheng, and C. Chan, Nature materials **10**, 582 (2011).

[15] Y. Li, S. Kita, P. Muñoz, O. Reshef, D. I. Vulis, M. Yin, M. Lončar, and E. Mazur, Nature Photonics **9**, 738 (2015).

[16] R. A. Vicencio, C. Cantillano, L. Morales-Inostroza, B. Real, C. Mejía-Cortés, S. Weimann, A. Szameit, and M. I. Molina, Physical review letters **114**, 245503 (2015).

[17] S. Mukherjee, A. Spracklen, D. Choudhury, N. Goldman, P. Öhberg, E. Andersson, and R. R. Thomson, Physical review letters **114**, 245504 (2015).

[18] D. Leykam, A. Andreanov, and S. Flach, Advances in Physics: X **3**, 1473052 (2018).

[19] E. Illes, Ph.D. thesis (2017).

[20] E. Illes and E. Nicol, Physical Review B **94**, 125435 (2016).

[21] E. Illes, J. P. Carbotte, and E. J. Nicol, Phys. Rev. B **92**, 245410 (2015).

[22] B. Dey and T. K. Ghosh, Physical Review B **98**, 075422 (2018).

[23] T. Biswas and T. K. Ghosh, Journal of Physics: Condensed Matter **30**, 075301 (2018).

[24] T. Biswas and T. K. Ghosh, Journal of Physics: Condensed Matter **28**, 495302 (2016).

[25] S. F. Islam and P. Dutta, Phys. Rev. B **96**, 045418 (2017).

[26] A. D. Kovács, G. Dávid, B. Dóra, and J. Cserti, Phys. Rev. B **95**, 035414 (2017).

[27] F. Piéchon, J. Fuchs, A. Raoux, and G. Montambaux, in *Journal of Physics: Conference Series* (IOP Publishing, 2015), vol. 603, p. 012001.

[28] B. Dey and T. K. Ghosh, Physical Review B **99**, 205429 (2019).

[29] C. J. Tabert and E. J. Nicol, Physical Review B **89**, 195410 (2014).

[30] M. Katsnelson, K. Novoselov, and A. Geim, Nature physics **2**, 620 (2006).

[31] E. Illes and E. Nicol, Physical Review B **95**, 235432 (2017).

[32] G. Gumbs, A. Iurov, D. Huang, and L. Zhemchuzhna, Physical Review B **89**, 241407 (2014).

[33] E. Gorbar, V. Gusynin, and D. Oriekhov, Physical Review B **99**, 155124 (2019).

[34] T. Low, R. Roldán, H. Wang, F. Xia, P. Avouris, L. M. Moreno, and F. Guinea, Physical review letters **113**, 106802 (2014).

[35] S. Soleimanikahnoj and I. Knezevic, Journal of Computational Electronics **16**, 568 (2017).

[36] T. Smoleński, M. Goryca, M. Koperski, C. Faugeras, T. Kazimierczuk, A. Bogucki, K. Nogajewski, P. Kossacki, and M. Potemski, Physical Review X **6**, 021024 (2016).

[37] Y. Fan, N.-H. Shen, F. Zhang, Q. Zhao, H. Wu, Q. Fu, Z. Wei, H. Li, and C. M. Soukoulis, Advanced Optical Materials **7**, 1800537 (2019).

[38] P. Perez-Piskunow, G. Usaj, C. Balseiro, and L. F. Torres, Physical Review B **89**, 121401 (2014).

[39] H. L. Calvo, H. M. Pastawski, S. Roche, and L. E. F. Torres, Applied Physics Letters **98**, 232103 (2011).

[40] E. S. Morell and L. E. F. Torres, Physical Review B **86**, 125449 (2012).

[41] Z. Gu, H. Fertig, D. P. Arovas, and A. Auerbach, Physical review letters **107**, 216601 (2011).

[42] V. Dal Lago, E. S. Morell, and L. F. Torres, Physical Review B **96**, 235409 (2017).

[43] G. Usaj, P. Perez-Piskunow, L. F. Torres, and C. Balseiro, Physical Review B **90**, 115423 (2014).

[44] I. Iorsh, K. Dini, O. Kibis, and I. Shelykh, Physical Review B **96**, 155432 (2017).

[45] N. Goldman and J. Dalibard, Physical review X **4**, 031027 (2014).

[46] O. Kibis, Physical Review B **81**, 165433 (2010).

[47] A. Iurov, G. Gumbs, O. Roslyak, and D. Huang, Journal of Physics: Condensed Matter **24**, 015303 (2011).

[48] O. Kibis, K. Dini, I. Iorsh, and I. Shelykh, Physical Review B **95**, 125401 (2017).

[49] O. Kibis, K. Dini, I. Iorsh, and I. Shelykh, Semiconductors **52**, 523 (2018).

[50] O. Kyriienko, O. Kibis, and I. Shelykh, Physical Review B **99**, 115411 (2019).

[51] A. Iurov, G. Gumbs, D. Huang, and L. Zhemchuzhna, Journal of Applied Physics **121**, 084306 (2017).

[52] A. Iurov, G. Gumbs, and D. Huang, Journal of Modern Optics **64**, 913 (2017).

[53] S. Morina, K. Dini, I. V. Iorsh, and I. A. Shelykh, ACS Photonics **5**, 1171 (2018).

[54] S. Morina, O. V. Kibis, A. A. Pervishko, and I. A. Shelykh, Phys. Rev. B **91**, 155312 (2015).

[55] K. Kristinsson, O. Kibis, S. Morina, and I. Shelykh, Scientific reports **6**, 20082 (2016).

[56] P. Pyatkovskiy, Journal of Physics: Condensed Matter **21**, 025506 (2008).

[57] A. Iurov, L. Zhemchuzhna, G. Gumbs, and D. Huang, Journal of Applied Physics **122**, 124301 (2017).

[58] A. Iurov, G. Gumbs, and D. Huang, Physical Review B **99**, 205135 (2019).

[59] V. Kozin, I. Iorsh, O. Kibis, and I. Shelykh, Physical Review B **97**, 035416 (2018).

[60] A. Politano and G. Chiarello, Nanoscale **6**, 10927 (2014).

[61] B. Wunsch, T. Stauber, F. Sols, and F. Guinea, New Journal of Physics **8**, 318 (2006).

[62] A. Scholz, T. Stauber, and J. Schliemann, Physical Review B **88**, 035135 (2013).

[63] G. Gumbs, A. Balassis, A. Iurov, and P. Fekete, The Scientific World Journal **2014** (2014).

[64] J. Tempere, I. F. Silvera, and J. T. Devreese, Phys. Rev. B **65**, 195418 (2002).

[65] A. Iurov, G. Gumbs, B. Gao, and D. Huang, Applied Physics Letters **104**, 203103 (2014).

[66] D. Huang, A. Iurov, H.-Y. Xu, Y.-C. Lai, and G. Gumbs, Physical Review B **99**, 245412 (2019).

[67] A. Iurov, G. Gumbs, and D. Huang, Physical Review B **98**, 075414 (2018).

[68] L. A. Falkovsky and S. S. Pershoguba, Phys. Rev. B **76**, 153410 (2007).

[69] T. Ando, A. B. Fowler, and F. Stern, Reviews of Modern Physics **54**, 437 (1982).

[70] E. Hwang and S. D. Sarma, Physical Review B **79**, 165404 (2009).

[71] A. C. Neto, F. Guinea, N. M. Peres, K. S. Novoselov, and A. K. Geim, Reviews of modern physics **81**, 109 (2009).

[72] E. H. Hwang and S. Das Sarma, Phys. Rev. B **77**, 195412 (2008).